Chemical Science

ROYAL SOCIETY OF CHEMISTRY

EDGE ARTICLE

View Article Online
View Journal | View Issue

Cite this: *Chem. Sci.*, 2025, **16**, 22387

All publication charges for this article have been paid for by the Royal Society of Chemistry

Wrapping a single crystal spin-crossover complex with a single crystal non-spin-crossover complex to modulate the spin-transition temperature

Tomoya Fukui, *[abc] Masahiro Tsuchiya,[ab] Naoya Mita[ab] and Takanori Fukushima [abc]

Received 12th June 2025
Accepted 24th October 2025

DOI: 10.1039/d5sc04311e

rsc.li/chemical-science

The formation of a heterojunction interface between different materials could lead to emergent functions that are not the simple sum of the properties of each component. Here we report the modulation of physical properties due to the lattice mismatch between two molecular crystals. Using metal complexes as a motif, we created a crystalline object that can be referred to as a core–shell crystal, in which a single crystal of one complex (Fe^{II} complex) is wrapped with a single crystal of a different complex (Co^{II} or Zn^{II} complex). X-ray analysis revealed that the Fe^{II} complex constituting the inner core exhibits spin-crossover behavior, while the Co^{II} (or Zn^{II}) complex constituting the outer shell does not. The crystal structure of the outer shell is different from that formed through spontaneous crystallization of the Co^{II} (or Zn^{II}) complex alone, but similar to that of the high-temperature phase of the spin-crossover Fe^{II} complex. Interestingly, the spin transition behavior of the Fe^{II} complex inside the core–shell crystals changes, demonstrating that in molecular materials, the formation of a heterojunction interface can modulate the properties of the entire bulk crystal. The fabrication of a ternary core–shell crystal using Fe^{II}, Co^{II} and Zn^{II} complexes is also presented.

Introduction

It is well known that in epitaxially grown films of inorganic materials, the lattice mismatch between two compounds leads to modulation of the physical properties of the material deposited on the substrate.[1–3] Does this hold true for molecular crystals? This question appears to be non-trivial, since unlike inorganic materials in which atoms are infinitely connected by strong chemical bonds, these materials consist of discrete molecules assembled together by weak intermolecular forces. It is interesting to consider whether, for example, if two different molecular crystals were brought into close contact, the structural information of each component could influence the other, causing a change in the overall properties. In reality, however, it is not easy to create a material in which two types of molecular crystals are closely linked together at the molecular level. This is because the lattice mismatch between dissimilar molecular crystals is too large due to the complexity and anisotropy of their components. Hence, when growing crystals from a solution of a mixture of two compounds, fractional recrystallization usually occurs.

In the past, there have been several reports on the construction of heterostructures using metal–organic frameworks (MOFs),[4–7] π-electronic molecules[8–10] and metal complexes[11–13] as constituents. However, little attention has been paid to the effect of lattice mismatches at heterojunction interfaces on the physical properties. In the present work, to create an elaborate heterojunction interface between two molecular crystals, we used metal complexes, which allow control over the physical properties without significantly changing the molecular structure by fixing the ligand while changing the type of metal ion. To explore the changes in physical properties due to the formation of heterojunction interfaces, we focused on the spin-crossover phenomenon, in which the spin state of a metal complex changes in response to external stimuli such as heat and light.[14–17] Previous studies on nanoscale core–shell spin-crossover systems have reported that interfacial lattice strain can modulate the spin-transition temperature.[18–24] However, this phenomenon has yet to be experimentally demonstrated in macroscopic single crystals. In the present work, we address this gap by demonstrating that even a small fraction of a heterojunction interface within a bulk crystal can modulate its overall spin-crossover behavior.

The above material design concept was embodied using metal complexes ligated with 4-carboxy-2,6-di(pyrazol-1-yl)

[a]*Laboratory for Chemistry and Life Science, Institute of Integrated Research, Institute of Science Tokyo, 4259 Nagatsuta, Midori-ku, Yokohama 226-8501, Japan. E-mail: fukui@cls.iir.isct.ac.jp*

[b]*Department of Chemical Science and Engineering, School of Materials and Chemical Technology, Institute of Science Tokyo, 4259 Nagatsuta, Midori-ku, Yokohama 226-8501, Japan*

[c]*Research Center for Autonomous Systems Materialogy (ASMat), Institute of Integrated Research, Institute of Science Tokyo, 4259 Nagatsuta, Midori-ku, Yokohama 226-8501, Japan*

pyridine[25,26] (cdpp) with compositions of $[M(cdpp)_2](BF_4)_2$ [$\mathbf{M_{cdpp}}$ (M = Fe, Co, Zn), Fig. 1]. $\mathbf{Fe_{cdpp}}$ undergoes a first-order phase transition between a low-spin state [total spin quantum number (S) = 0] and a high-spin state (S = 2) as the low-temperature and high-temperature phases, respectively, accompanied by a change in the molecular structure.[25,26] On the other hand, $\mathbf{Co_{cdpp}}$ has only a high-spin state (S = 3/2), and $\mathbf{Zn_{cdpp}}$ is diamagnetic in nature (S = 0), with both of them exhibiting no first-order phase transitions. We created a crystalline object that can be referred to as a core–shell crystal, in which a single crystal of $\mathbf{Fe_{cdpp}}$ is wrapped with a single crystal of $\mathbf{Co_{cdpp}}$ or $\mathbf{Zn_{cdpp}}$. A key to the successful formation of such core–shell crystals ($\mathbf{Fe_{cdpp}@Co_{cdpp}}$ and $\mathbf{Fe_{cdpp}@Zn_{cdpp}}$, Fig. 1b) lies in the seeded crystal growth method, which has been used to construct block supramolecular assemblies[27–32] and block crystallizable polymer-based micelles.[33–36] Interestingly, in this seeded crystallization, the crystal structure of $\mathbf{Co_{cdpp}}$ or $\mathbf{Zn_{cdpp}}$ that forms the outer shell is different from that when it crystallizes alone. What is even more interesting is that the spin transition temperature of the $\mathbf{Fe_{cdpp}}$ core changes, where the greater the lattice mismatch between the core and shell crystals, the lower the spin transition temperature. Here we report the preparation, crystal structures and spin-crossover behavior of these core–shell crystals. The fabrication and characterization of a ternary core–shell crystal ($\mathbf{Fe_{cdpp}@Co_{cdpp}@Zn_{cdpp}}$, Fig. 1b) is also described.

Results and discussion

Preparation and characterization of single crystals of $\mathbf{M_{cdpp}}$

The 4-carboxy-2,6-di(pyrazol-1-yl)pyridine (cdpp) ligand was synthesized according to previously reported procedures.[37] Single crystals of $\mathbf{M_{cdpp}}$ (M = Fe, Co, Zn) were prepared using a liquid–liquid diffusion crystallization method (Fig. S1, SI). Typically, an acetonitrile solution of a mixture of cdpp (1.0 eq.) and $Fe(BF_4)_2\cdot 6H_2O$ (0.5 eq.) is layered on top of a highly concentrated acetonitrile solution (6.6 M) of tetrabutylammonium tetrafluoroborate ($TBABF_4$) and allowed to stand at 25 °C for two days, leading to the formation of single crystals of $\mathbf{Fe_{cdpp}}$ (Fig. 2a). By following a similar procedure as for $\mathbf{Fe_{cdpp}}$, except that $Co(BF_4)_2\cdot 6H_2O$ (0.5 eq.) or $Zn(BF_4)_2\cdot nH_2O$ (0.5 eq.) are used instead of $Fe(BF_4)_2\cdot 6H_2O$, single crystals of $\mathbf{Co_{cdpp}}$ or $\mathbf{Zn_{cdpp}}$ can be prepared (Fig. 2b and c).

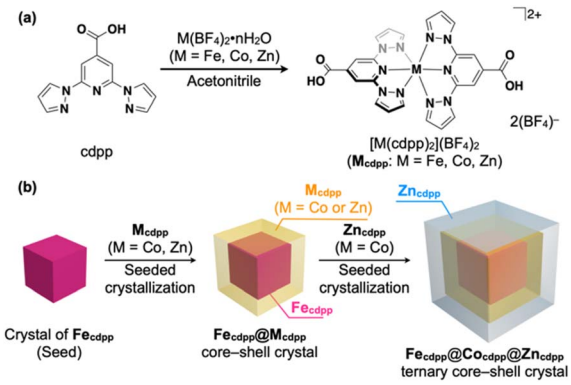

Fig. 1 (a) Synthetic scheme of M_{cdpp} (M = Fe, Co, Zn). cdpp: 4-carboxy-2,6-di(pyrazol-1-yl)pyridine. (b) Schematic illustration of core–shell crystals of M_{cdpp} using a seeded crystal growth method.

Fig. 2 shows the X-ray crystal structures of $\mathbf{Fe_{cdpp}}$, $\mathbf{Co_{cdpp}}$ and $\mathbf{Zn_{cdpp}}$ at 93 K, along with polarized optical micrographs (POM) of single crystal samples for each complex. The single crystal of $\mathbf{Fe_{cdpp}}$ belongs to a monoclinic system with space group $C2/c$ (Fig. 2a). $\mathbf{Fe_{cdpp}}$ has an average Fe–N bond length (d_{Fe-N}) of 1.946 Å and an octahedral distortion parameter (Σ) of 85.32°. These values are typical for low-spin state Fe^{II} complexes.[14–16,25,26] In terms of packing structure, the $\mathbf{Fe_{cdpp}}$ molecules assemble to form a one-dimensional (1D) hydrogen-bonded chain structure along the b-axis. When single crystalline $\mathbf{Fe_{cdpp}}$ is heated, it undergoes a phase transition involving a spin crossover with a change from a low- to a high-spin state. Thus, as determined from the X-ray crystal structure, the values of d_{Fe-N} (1.946 Å) and Σ (85.32°) at 93 K change at 393 K to 2.156 Å and 163.1°, respectively (Fig. S2, SI).

$\mathbf{Co_{cdpp}}$ crystallizes into an orthorhombic system with space group *Pbcn*, in which a 1D hydrogen-bonded chain structure of $\mathbf{Co_{cdpp}}$ is formed along the a-axis (Fig. 2b). In the crystal, the average Co–N bond length (d_{Co-N}) of $\mathbf{Co_{cdpp}}$ is 2.122 Å, and its Σ value is 135.4°, indicating that $\mathbf{Co_{cdpp}}$ is in a high-spin state.[38] Likewise, $\mathbf{Zn_{cdpp}}$ crystallizes into an orthorhombic space group (*Pbcn*), and the packing structure of the $\mathbf{Zn_{cdpp}}$ molecules is almost identical to that observed for single-crystalline $\mathbf{Co_{cdpp}}$ (Fig. 2c).

Preparation and characterization of core–shell crystals

Using single crystals of the spin-crossover $\mathbf{Fe_{cdpp}}$ complex as seeds, we examined crystal growth of the $\mathbf{Co_{cdpp}}$ complex from the seed surface (Fig. S1, SI). Thus, single crystals of $\mathbf{Fe_{cdpp}}$ [number-average area (A_n) = 8.07 × 10^3 μm^2 and dispersity index (A_w/A_n) = 1.04] were immersed in an acetonitrile solution (6.6 M) of $TBABF_4$. On top of this, a saturated acetonitrile solution of $\mathbf{Co_{cdpp}}$ was layered slowly. After two days, core–shell crystals (denoted hereafter as $\mathbf{Fe_{cdpp}@Co_{cdpp}}$) were formed (Fig. 3a). An optical micrograph of the resulting crystals illustrates that the $\mathbf{Fe_{cdpp}}$ seed crystals are covered with an outer shell of crystalline $\mathbf{Co_{cdpp}}$ (Fig. S3, SI), indicating quantitative formation of $\mathbf{Fe_{cdpp}@Co_{cdpp}}$ (A_n = 1.21 × 10^4 μm^2 and A_w/A_n = 1.02). Scanning electron microscopy energy dispersive X-ray spectroscopy (SEM-EDX) of $\mathbf{Fe_{cdpp}@Co_{cdpp}}$ confirmed that the Fe content in the outer shell is below the detection limit (Fig. 3b). For analysis of the inner core, a $\mathbf{Fe_{cdpp}@Co_{cdpp}}$ crystal was embedded in an epoxy resin and sliced using an ultramicrotome. The SEM-EDX profile of a sliced sample of $\mathbf{Fe_{cdpp}@Co_{cdpp}}$ shows the presence of a distinct heterojunction interface between the $\mathbf{Fe_{cdpp}}$ core and the $\mathbf{Co_{cdpp}}$ shell (Fig. 3c). These results demonstrate the formation of core–shell crystals having well-defined heterojunction interfaces.

When the seeded crystallization event was monitored in real time, the formation of $\mathbf{Fe_{cdpp}@Co_{cdpp}}$ was observed after leaving the two-layer solution to stand for about 5 h (Fig. S4, SI), which is faster than the spontaneous crystallization of $\mathbf{Co_{cdpp}}$ (about

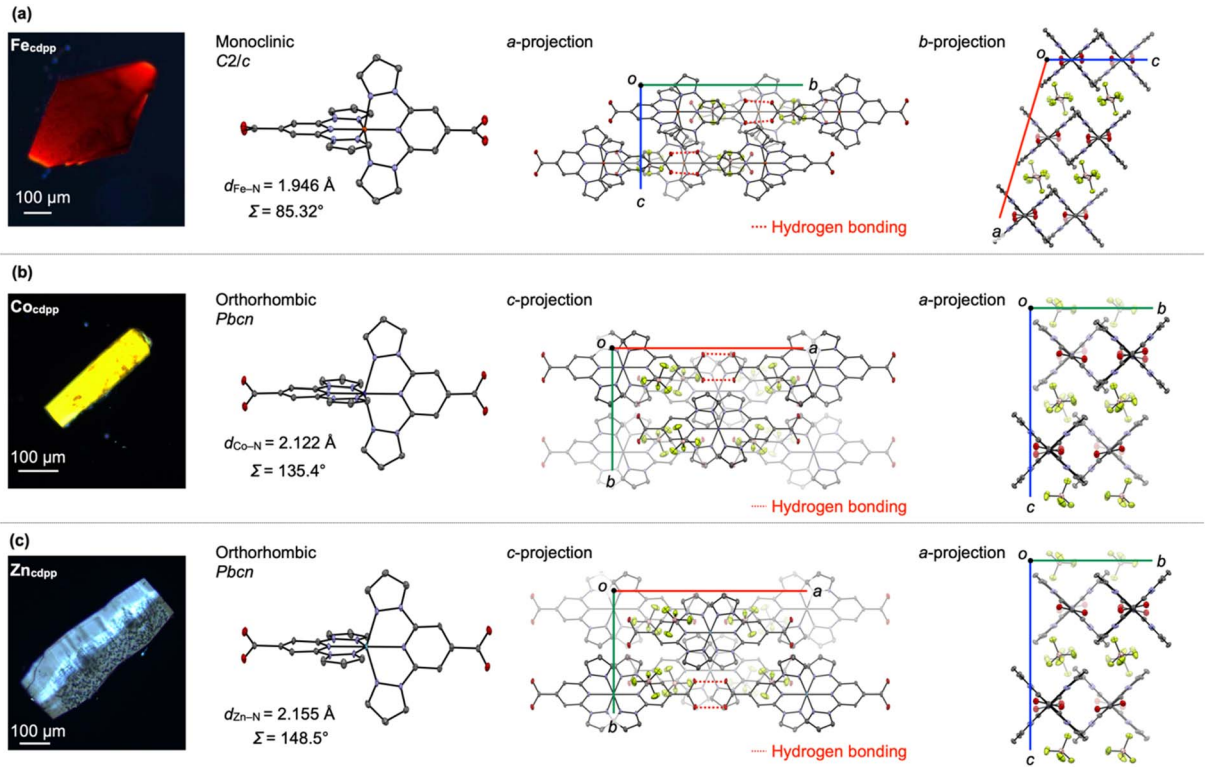

Fig. 2 POM images and X-ray crystal structures (molecular and packing structures) of (a) Fe_{cdpp}, (b) Co_{cdpp} and (c) Zn_{cdpp}. Color code: carbon = gray, nitrogen = blue, oxygen = red, iron = orange, cobalt = purple, zinc = sky blue, fluorine = green, boron = pink. Hydrogen atoms have been omitted for clarity.

20 h) without seeds under otherwise identical conditions (Fig. S5, SI). Thus, the surface of the seed Fe_{cdpp} crystal may provide kinetic perturbation in the crystallization of Co_{cdpp}.

The inner core and outer shell of the crystals were cut out and each segment analyzed by single-crystal X-ray analysis at 93 K. As expected, before and after the seeded crystal growth

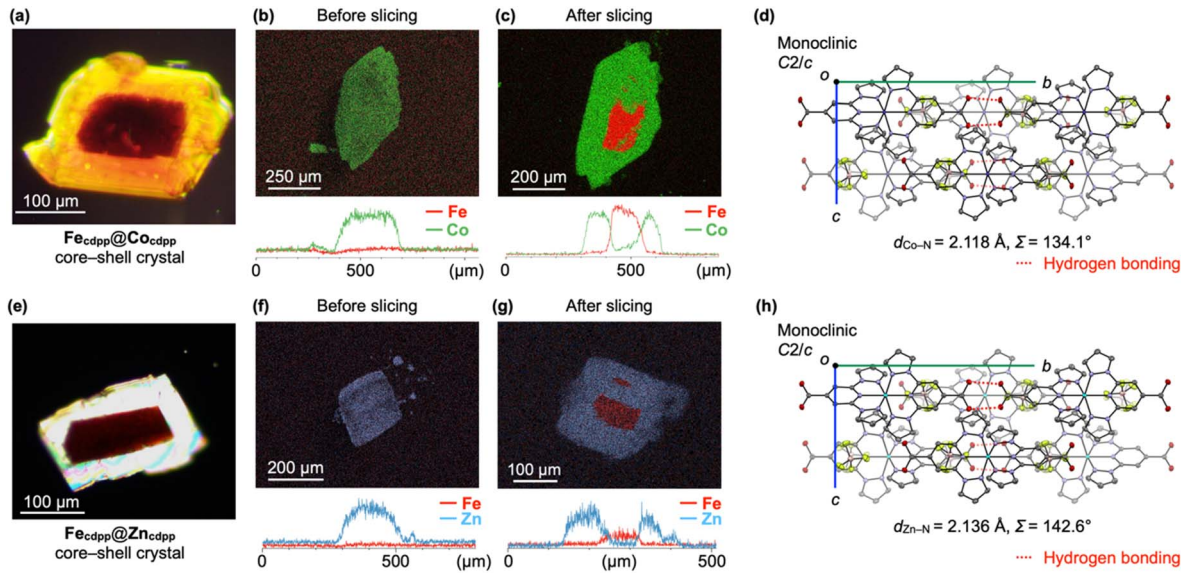

Fig. 3 (a) POM image of Fe_{cdpp}@Co_{cdpp}. (b and c) SEM-EDX elemental maps (top) and total area traces (bottom) of Fe_{cdpp}@Co_{cdpp} (b) before and (c) after slicing by a ultramicrotome. (d) Crystal structure of Co_{cdpp} in the outer shell along the *a*-axis. (e) POM image of Fe_{cdpp}@Zn_{cdpp}. (f and g) SEM-EDX elemental maps (top) and total area traces (bottom) of Fe_{cdpp}@Zn_{cdpp} (f) before and (g) after slicing by a ultramicrotome. (h) Crystal structure of Zn_{cdpp} in the outer shell along the *a*-axis.

process, the crystal structure of the core **Fe$_{cdpp}$** remains unchanged. On the other hand, the crystal structure of the **Co$_{cdpp}$** shell is different from when **Co$_{cdpp}$** crystallizes alone in acetonitrile (Fig. 2b), and instead, it inherits the structural feature of the core **Fe$_{cdpp}$** (Fig. 3d and S6, SI). Thus, the **Co$_{cdpp}$** forming the outer shell has the space group *C*2/*c*, where the difference in lattice constant with the core **Fe$_{cdpp}$** is within a range of 2.5% or less (Table S1, SI). This suggests that on the surface of the **Fe$_{cdpp}$** seed crystal, a kinetic assembly of **Co$_{cdpp}$** is induced, which grows to become the outer shell. Notably, optical microscopy (OM) and scanning electron microscopy (SEM) have not shown any seams on the surfaces or edges of the core–shell crystals (Fig. S3 and S7, SI). In POM (Fig. S8, SI), the molecular orientations in the core and shell of **Fe$_{cdpp}$@Co$_{cdpp}$** are identical to each other. These observations indicate that **Fe$_{cdpp}$@Co$_{cdpp}$** is formed through a topotactic crystal growth process,[39,40] resulting in a core–shell type "pseudo-single crystal" with two distinct well-defined domains.

Despite the difference in crystal structure and space group, there is no significant difference in the molecular structure of **Co$_{cdpp}$** in the crystal formed in the absence or presence of the **Fe$_{cdpp}$** seed. For example, the values of d_{Co-N} (2.118 Å) and Σ (134.1°) are virtually identical to those observed in the **Co$_{cdpp}$** crystal alone (d_{Co-N} = 2.122 Å and Σ = 135.4°), indicating that the **Co$_{cdpp}$** shell crystal is in the high-spin state.[38]

Similar to **Fe$_{cdpp}$@Co$_{cdpp}$**, using single crystals of **Fe$_{cdpp}$** ($A_n = 3.63 \times 10^3$ μm^2) as seeds, crystals of **Zn$_{cdpp}$** can grow around them (Fig. 3e). The resulting core–shell crystals, **Fe$_{cdpp}$@Zn$_{cdpp}$** ($A_n = 6.05 \times 10^3$ μm^2 and $A_w/A_n = 1.06$), have been unambiguously characterized by SEM-EDX (Fig. 3f and g) and single-crystal X-ray analysis (Fig. 3h and S9, SI). The **Zn$_{cdpp}$** shell of **Fe$_{cdpp}$@Zn$_{cdpp}$** adopts the *C*2/*c* space group (Fig. 3h), while crystals with the *Pbcn* space group grow from an acetonitrile solution of **Zn$_{cdpp}$** alone (Fig. 2c). The difference in lattice constant with the core **Fe$_{cdpp}$** is within a range of 3.1% or less (Table S1, SI). As in the case of **Fe$_{cdpp}$@Co$_{cdpp}$**, the **Zn$_{cdpp}$** shell inherits the structural feature of the core **Fe$_{cdpp}$** (Fig. 3h and S9, SI).

Unfortunately, attempts to crystallize the **Fe$_{cdpp}$** complex from the seed surface of either **Co$_{cdpp}$** or **Zn$_{cdpp}$** have not been successful. Presumably, **Fe$_{cdpp}$** would be unable to give *Pbcn* space group crystals as a kinetic form on the **Co$_{cdpp}$** and **Zn$_{cdpp}$** crystal surfaces.

Spin-crossover behavior of core–shell crystals

Since spin-crossover is a first-order phase transition involving structural changes,[14–16] its occurrence can be detected using differential scanning calorimetry (DSC) measurements. Prior to DSC measurements, we confirmed by thermogravimetric analysis (TGA) that all samples are thermally stable up to approximately 450 K, with no significant weight loss within the experimental temperature range (Fig. S10, SI). Fig. 4a shows the DSC profiles of **Fe$_{cdpp}$**, **Fe$_{cdpp}$@Co$_{cdpp}$** and **Fe$_{cdpp}$@Zn$_{cdpp}$**. Upon heating from 223 K at a rate of 1 K min^{-1}, **Fe$_{cdpp}$** exhibits an endothermic peak at 348 K due to a spin-crossover phenomenon. At the same temperature, the colour of the crystals

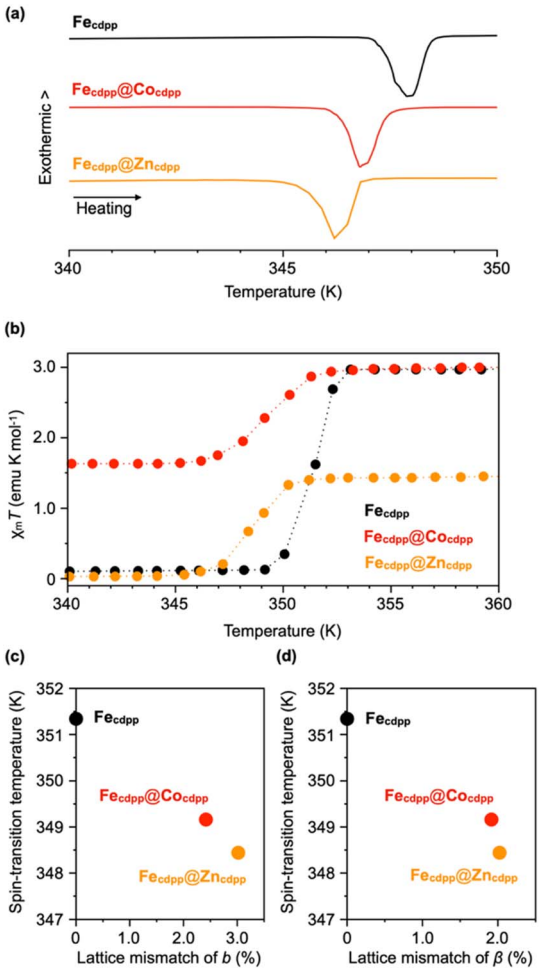

Fig. 4 (a) DSC profiles of **Fe$_{cdpp}$** (black), **Fe$_{cdpp}$@Co$_{cdpp}$** (red) and **Fe$_{cdpp}$@Zn$_{cdpp}$** (orange) upon heating at a rate of 1 K min^{-1}. (b) Temperature-dependent magnetic susceptibility of **Fe$_{cdpp}$** (black), **Fe$_{cdpp}$@Co$_{cdpp}$** (red) and **Fe$_{cdpp}$@Zn$_{cdpp}$** (orange) upon heating at a rate of 1 K min^{-1} under a magnetic field of 1 T (see Fig. S13 for the cooling process, SI). The χ_mT values were calculated assuming a 50 : 50 molar ratio between **Fe$_{cdpp}$** and **M$_{cdpp}$** (M = Co, Zn) in the core–shell crystals. Plots of spin-transition temperatures ($T_{1/2}$) *versus* core/shell lattice constant mismatch at (c) *b* and (d) *β*.

changes from red to orange (Fig. S11, SI). Similarly, **Fe$_{cdpp}$@Co$_{cdpp}$** and **Fe$_{cdpp}$@Zn$_{cdpp}$** undergo spin-crossover, with the appearance of endothermic peaks at 347 K and 346 K, respectively. While the difference in phase transition temperature is rather small, a clear difference can be observed between **Fe$_{cdpp}$** and the core–shell crystals. OM visualized the colour change occurring only in the cores of **Fe$_{cdpp}$@Co$_{cdpp}$** and **Fe$_{cdpp}$@Zn$_{cdpp}$** (Fig. S11, SI).[41,42] For comparison, we also measured DSC of a sample in which **Fe$_{cdpp}$** single crystals are wrapped in an epoxy resin and confirmed that there is no change in the phase transition temperature associated with the spin crossover of **Fe$_{cdpp}$** (Fig. S12, SI).

Using a superconducting quantum interference device (SQUID) magnetometer, we investigated the temperature-dependence of the magnetic susceptibility of **Fe$_{cdpp}$**, **Fe$_{cdpp}$@Co$_{cdpp}$** and **Fe$_{cdpp}$@Zn$_{cdpp}$**, upon heating from 4 K at a rate of 1

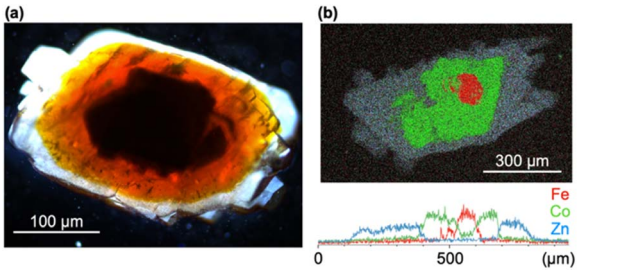

Fig. 5 (a) POM image of $Fe_{cdpp}@Co_{cdpp}@Zn_{cdpp}$. (b) SEM-EDX elemental map and total area trace along one axis of $Fe_{cdpp}@Co_{cdpp}@Zn_{cdpp}$ after slicing by a ultramicrotome. Color code: iron = red, cobalt = green, zinc = sky blue.

K min^{-1} under an external magnetic field of 1 T (Fig. 4b). Each SQUID measurement was repeated twice independently, which confirmed the reproducibility of the data. Consistent with previous reports,[25,26] we observed that the $\chi_m T$ value of **Fe_{cdpp}** abruptly increases to 3.0 emu K mol^{-1} with a spin-transition temperature ($T_{1/2}$) of 351 K, which is due to spin-crossover from the low- ($S = 0$) to high-spin state ($S = 2$). For **$Fe_{cdpp}@Co_{cdpp}$**, the $\chi_m T$ value below 345 K was determined to be approximately 1.6 emu K mol^{-1}, reflecting both high-spin state of **Co_{cdpp}** ($S = 3/2$) and low-spin state of **Fe_{cdpp}** ($S = 0$). The $\chi_m T$ value greatly increases to 3.0 emu K mol^{-1} due to the spin-crossover behavior of the core **Fe_{cdpp}** with $T_{1/2}$ of 349 K. **$Fe_{cdpp}@Zn_{cdpp}$** also displays spin-crossover behavior with $T_{1/2}$ of 348 K (Fig. 4b). The fact that the $T_{1/2}$ values for **$Fe_{cdpp}@Co_{cdpp}$** (349 K) and **$Fe_{cdpp}@Zn_{cdpp}$** (348 K) are similar but apparently lower than that for **Fe_{cdpp}** ($T_{1/2} = 351$ K) shows that the wrapping of crystalline **Fe_{cdpp}** with other complex crystals perturbs the original spin-crossover behavior. It has been reported that the high-spin state of Fe^{II} complexes is stabilized in solid-solution systems diluted with Ni^{II}, Co^{II}, or Zn^{II} ions, which have ionic radii similar to that of Fe^{II} in the high-spin state.[43–45] However, it is notable that the phase-transition behavior of the entire bulk crystal changes when spatially distinct crystalline domains are closely linked together.

We found that the degree of lattice constant mismatch of each block segment is related to $T_{1/2}$. In **$Fe_{cdpp}@Co_{cdpp}$**, when comparing the values of b and β between the **Fe_{cdpp}** core and the **Co_{cdpp}** shell, there are differences of 2.42% and 1.91%, respectively (Fig. S14 and Table S1, SI). **$Fe_{cdpp}@Zn_{cdpp}$** has differences in b and β of 3.02% and 2.02%, respectively (Table S1, SI), which are slightly larger than the case of **$Fe_{cdpp}@Co_{cdpp}$**. Clearly, the greater the lattice mismatch between the core and shell crystals, the lower the spin transition temperature (Fig. 4c, d and S15, SI). It should be noted that the values of b and β of **Co_{cdpp}** and **Zn_{cdpp}**, which form the outer shell, are closer to those of the high temperature phase of **Fe_{cdpp}** (*i.e.*, high-spin state), than to those of its low temperature phase (*i.e.*, low-spin state).

Since the interface of the core–shell crystals would be in a higher energy state than the interior of the **Fe_{cdpp}** core, the phase transition is thought to be initiated from the interface. The interface is covered by the crystalline shell of **Co_{cdpp}** or **Zn_{cdpp}** with a structure similar to the high-temperature phase of **Fe_{cdpp}**. That is, for the low-temperature phase of **Fe_{cdpp}** before the transition, the shell has a structural mismatch, while for the high-temperature phase of **Fe_{cdpp}** generating after the transition, the shell has a structural similarity. This feature of the heterojunction interface is considered responsible for lowering the phase transition temperature in the core–shell crystal systems. In fact, the structure of the shell **Zn_{cdpp}** is more similar to the high-temperature phase of **Fe_{cdpp}** than that of the **Co_{cdpp}** shell, and **$Fe_{cdpp}@Zn_{cdpp}$** undergoes the phase transition at a lower temperature than **$Fe_{cdpp}@Co_{cdpp}$**. Such interfacial effects have also been discussed previously in nanoscale coordination polymer core–shell systems, where the modulation of spin-transition behavior is understood in terms of elastic effects due to a mismatch in lattice parameters at the interface.[18–24] The present results may extend this nanoscale understanding to macroscopic core–shell structures composed of molecular crystals.

Preparation and characterization of a ternary core–shell crystal

We have shown that sequential seeded crystallization allows for the preparation of an intriguing ternary core–shell crystals. As mentioned above, crystalline **Co_{cdpp}** and **Zn_{cdpp}** can be grown from the surface of a seed crystal of **Fe_{cdpp}**, and also both can form a crystal structure with the monoclinic $C2/c$ space group. Taking advantage of these structuring properties, **$Fe_{cdpp}@Co_{cdpp}@Zn_{cdpp}$** can be obtained through the sequential seeded crystallization of **Co_{cdpp}** and **Zn_{cdpp}** from a single crystal of **Fe_{cdpp}** as seed (Fig. 1b). The ternary core–shell crystals have been characterized by OM and SEM-EDX (Fig. 5a, b and S16, SI). In DSC, **$Fe_{cdpp}@Co_{cdpp}@Zn_{cdpp}$**, upon heating, exhibits an endothermic peak at 347 K (Fig. S12, SI), which is the same as in the case of **$Fe_{cdpp}@Co_{cdpp}$**. As expected, the phase transition behavior of the core **Fe_{cdpp}** is affected only by the outer shells in direct contact with it.

Conclusions

We have presented the preparation and characterization of core–shell crystals, in which a single crystal spin-crossover complex (**Fe_{cdpp}**) is wrapped with a single crystal of a non-spin-crossover metal complex (**Co_{cdpp}** or **Zn_{cdpp}**), using the seeded crystallization approach. Interestingly, the crystal structures of the **Co_{cdpp}** and **Zn_{cdpp}** shells are different from those formed by their spontaneous crystallization, and instead they inherit the crystal structure of the inner **Fe_{cdpp}** core. When **Fe_{cdpp}** is surrounded by an outer shell of **Co_{cdpp}** or **Zn_{cdpp}**, its phase transition shifts to a lower temperature, with the degree of variation becoming larger the greater the similarity between the lattice constants of **Co_{cdpp}** or **Zn_{cdpp}**, and the structure of the high temperature phase of **Fe_{cdpp}**. In this seeded crystallization, the **Fe_{cdpp}** seed induces the outer shell complex to crystallize into a structure different from its intrinsic one, and thus indirectly tunes the inherent phase transition behavior. The present study, which demonstrates that a heterojunction interface in different molecular crystals can have a noticeable effect on the

physical properties of the bulk crystals, sparks new interest in the seeded crystallization approach to interface design of molecular crystals.

Author contributions

To. F. conceived the project; To. F. and Ta. F. designed the experiments; M. T., N. M. and To. F. carried out the experiments and analysed the data; To. F. and Ta. F. co-wrote the manuscript.

Conflicts of interest

There are no conflicts to declare.

Data availability

The data supporting this article have been included as part of the supplementary information (SI). The supplementary information includes crystal data, OM/POM images, TGA data, DSC profiles, SEM images and magnetic susceptibility data. See DOI: https://doi.org/10.1039/d5sc04311e.

CCDC 2214914 (for $\mathbf{Fe}_{\mathbf{cdpp}}$), 2408263 (for $\mathbf{Fe}_{\mathbf{cdpp}}$ at 393 K), 2214916 (for $\mathbf{Co}_{\mathbf{cdpp}}$), 2214918 (for $\mathbf{Zn}_{\mathbf{cdpp}}$), 2214915 (for $\mathbf{Co}_{\mathbf{cdpp}}$ in the shell) and 2214919 (for $\mathbf{Zn}_{\mathbf{cdpp}}$ in the shell) contain the supplementary crystallographic data for this paper.[46a–f]

Acknowledgements

This work was supported by Japan Science and Technology Agency (JST) ACT-X (JPMJAX24DH for To.F.), JSPS KAKENHI (JP23K13728 for To.F.) and Grant-in-Aid for Transformative Research Areas (A) "Supra-ceramics" (JP23H04617 for To.F.). This work was also supported by "Crossover Alliance to Create the Future with People, Intelligence and Materials" from MEXT, Japan. We thank the Materials Analysis Division, Core Facility Center, Institute of Science Tokyo, for their support with SEM-EDX and single-crystal X-ray diffraction measurements.

Notes and references

1 S. A. Chambers, *Surf. Sci. Rep.*, 2000, **39**, 105–180.
2 J. Mannhart and D. G. Schlom, *Science*, 2010, **327**, 1607–1611.
3 H. Y. Hwang, Y. Iwasa, M. Kawasaki, B. Keimer, N. Nagaosa and Y. Tokura, *Nat. Mater.*, 2012, **11**, 103–113.
4 S. Furukawa, K. Hirai, K. Nakagawa, Y. Takashima, R. Matsuda, T. Tsuruoka, M. Kondo, R. Haruki, D. Tanaka, H. Sakamoto, S. Shimomura, O. Sakata and S. Kitagawa, *Angew. Chem., Int. Ed.*, 2009, **48**, 1766–1770.
5 M. Pan, Y.-X. Zhu, K. Wu, L. Chen, Y.-J. Hou, S.-Y. Yin, H.-P. Wang, Y.-N. Fan and C.-Y. Su, *Angew. Chem., Int. Ed.*, 2017, **56**, 14582–14586.
6 C. Liu, Q. Sun, L. Lin, J. Wang, C. Zhang, C. Xia, T. Bao, J. Wan, R. Huang, J. Zou and C. Yu, *Nat. Commun.*, 2020, **11**, 4971.
7 K. Leng, H. Sato, Z. Chen, W. Yuan and T. Aida, *J. Am. Chem. Soc.*, 2023, **145**, 23416–23421.
8 M.-P. Zhuo, J.-J. Wu, X.-D. Wang, Y.-C. Tao, Y. Yuan and L.-S. Liao, *Nat. Commun.*, 2019, **10**, 3839.
9 Y. Su, B. Wu, S. Chen, J. Sun, Y. Yu, M. Zhuo, Z. Wang and X. Wang, *Angew. Chem., Int. Ed.*, 2022, **61**, e202117857.
10 Q. Lv, X.-D. Wang, Y. Yu, M.-P. Zhuo, M. Zheng and L.-S. Liao, *Nat. Commun.*, 2022, **13**, 3099.
11 C. R. R. Adolf, S. Ferlay, N. Kyritsakas and M. W. Hosseini, *J. Am. Chem. Soc.*, 2015, **137**, 15390–15393.
12 M. Wakizaka, S. Kumagai, H. Wu, T. Sonobe, H. Iguchi, T. Yoshida, M. Yamashita and S. Takaishi, *Nat. Commun.*, 2022, **13**, 1188.
13 Q. Wan, M. Wakizaka, N. Funakoshi, Y. Shen, C.-M. Che and M. Yamashita, *J. Am. Chem. Soc.*, 2023, **145**, 14288–14297.
14 M. A. Halcrow, *Chem. Soc. Rev.*, 2011, **40**, 4119–4142.
15 P. Guionneau, *Dalton Trans.*, 2013, **43**, 382–393.
16 G. Molnár, S. Rat, L. Salmon, W. Nicolazzi and A. Bousseksou, *Adv. Mater.*, 2018, **30**, 1703862.
17 M. Gavara-Edo, R. Córdoba, F. J. Valverde-Muñoz, J. Herrero-Martín, J. A. Real and E. Coronado, *Adv. Mater.*, 2022, **34**, e2202551.
18 L. Catala, D. Brinzei, Y. Prado, A. Gloter, O. Stéphan, G. Rogez and T. Mallah, *Angew. Chem., Int. Ed.*, 2008, **48**, 183–187.
19 C. M. Quintero, G. Félix, I. Suleimanov, J. S. Costa, G. Molnár, L. Salmon, W. Nicolazzi and A. Bousseksou, *Beilstein J. Nanotechnol.*, 2014, **5**, 2230–2239.
20 Y.-X. Wang, D. Qiu, S.-F. Xi, Z.-D. Ding, Z. Li, Y. Li, X. Ren and Z.-G. Gu, *Chem. Commun.*, 2016, **52**, 8034–8037.
21 H. Oubouchou, Y. Singh and K. Boukheddaden, *Phys. Rev. B*, 2018, **98**, 014106.
22 C. Felts, A. Slimani, J. M. Cain, M. J. Andrus, A. R. Ahir, K. A. Abboud, M. W. Meisel, K. Boukheddaden and D. R. Talham, *J. Am. Chem. Soc.*, 2018, **140**, 5814–5824.
23 K. Affes, A. Slimani, A. Maalej and K. Boukheddaden, *Chem. Phys. Lett.*, 2019, **718**, 46–53.
24 N. Natt and B. Powell, 2019, *ChemRxiv*, preprint, DOI: 10.26434/chemrxiv-2025-tgqb3.
25 A. Abhervé, M. Clemente-León, E. Coronado, C. J. Gómez-García and M. López-Jordà, *Dalton Trans.*, 2014, **43**, 9406–9409.
26 V. García-López, M. Palacios-Corella, A. Abhervé, I. Pellicer-Carreño, C. Desplanches, M. Clemente-León and E. Coronado, *Dalton Trans.*, 2018, **47**, 16958–16968.
27 B. Adelizzi, N. J. V. Zee, L. N. J. de Windt, A. R. A. Palmans and E. W. Meijer, *J. Am. Chem. Soc.*, 2019, **141**, 6110–6121.
28 W. Zhang, W. Jin, T. Fukushima, A. Saeki, S. Seki and T. Aida, *Science*, 2011, **334**, 340–343.
29 S. H. Jung, D. Bochicchio, G. M. Pavan, M. Takeuchi and K. Sugiyasu, *J. Am. Chem. Soc.*, 2018, **140**, 10570–10577.
30 W. Wagner, M. Wehner, V. Stepanenko and F. Würthner, *J. Am. Chem. Soc.*, 2019, **141**, 12044–12054.
31 Q. Wan, W.-P. To, X. Chang and C.-M. Che, *Chem*, 2020, **6**, 945–967.
32 N. Sasaki, J. Kikkawa, Y. Ishii, T. Uchihashi, H. Imamura, M. Takeuchi and K. Sugiyasu, *Nat. Chem.*, 2023, **15**, 922–929.

33 L. R. MacFarlane, H. Shaikh, J. D. Garcia-Hernandez, M. Vespa, T. Fukui and I. Manners, *Nat. Rev. Mater.*, 2021, **6**, 7–26.
34 Z. M. Hudson, D. J. Lunn, M. A. Winnik and I. Manners, *Nat. Commun.*, 2014, **5**, 3372.
35 H. Qiu, Z. M. Hudson, M. A. Winnik and I. Manners, *Science*, 2015, **347**, 1329–1332.
36 X.-H. Jin, M. B. Price, J. R. Finnegan, C. E. Boott, J. M. Richter, A. Rao, S. M. Menke, R. H. Friend, G. R. Whittell and I. Manners, *Science*, 2018, **360**, 897–900.
37 T. Vermonden, D. Branowska, A. T. M. Marcelis and E. J. R. Sudhölter, *Tetrahedron*, 2003, **59**, 5039–5045.
38 M. Nakaya, W. Kosaka, H. Miyasaka, Y. Komatsumaru, S. Kawaguchi, K. Sugimoto, Y. Zhang, M. Nakamura, L. F. Lindoy and S. Hayami, *Angew. Chem., Int. Ed.*, 2020, **59**, 10658–10665.
39 S. Kittaka, H. Hamaguchi, T. Umezu, T. Endoh and T. Takenaka, *Langmuir*, 1997, **13**, 1352–1358.
40 P. Zhang, T. Ochi, M. Fujitsuka, Y. Kobori, T. Majima and T. Tachikawa, *Angew. Chem., Int. Ed.*, 2017, **56**, 5299–5303.
41 F. Varret, A. Slimani, K. Boukheddaden, C. Chong, H. Mishra, E. Collet, J. Haasnoot and S. Pillet, *New J. Chem.*, 2011, **35**, 2333–2340.
42 M. Sy, D. Garrot, A. Slimani, M. Páez-Espejo, F. Varret and K. Boukheddaden, *Angew. Chem., Int. Ed.*, 2016, **55**, 1755–1759.
43 J.-P. Martin, J. Zarembowitch, A. Dworkin, J. G. Haasnoot and E. Codjovi, *Inorg. Chem.*, 1994, **33**, 2617–2623.
44 M. A. Halcrow, H. B. Vasili, C. M. Pask, A. N. Kulak and O. Cespedes, *Dalton Trans.*, 2024, **53**, 6983–6992.
45 M. A. Halcrow, *Dalton Trans.*, 2024, **53**, 13694–13708.
46 (*a*) CCDC 2214914: Experimental Crystal Structure Determination, 2025, DOI: **10.5517/ccdc.csd.cc2dbsvd**; (*b*) CCDC 2214915: Experimental Crystal Structure Determination, 2025, DOI: **10.5517/ccdc.csd.cc2dbswf**; (*c*) CCDC 2214916: Experimental Crystal Structure Determination, 2025, DOI: **10.5517/ccdc.csd.cc2dbsxg**; (*d*) CCDC 2214918: Experimental Crystal Structure Determination, 2025, DOI: **10.5517/ccdc.csd.cc2dbszj**; (*e*) CCDC 2214919: Experimental Crystal Structure Determination, 2025, DOI: **10.5517/ccdc.csd.cc2dbt0l**; (*f*) CCDC 2408263: Experimental Crystal Structure Determination, 2025, DOI: **10.5517/ccdc.csd.cc2ltzxb**.